CrossMark

A Near-half-century Simulation of the Solar Corona

Valentin Aslanyan[1] , Karen A. Meyer[1] , Roger B. Scott[2] , and Anthony R. Yeates[3]

[1] Division of Mathematics, School of Science and Engineering, University of Dundee, Dundee, DD1 4HN, UK; vaslanyan001@dundee.ac.uk

[2] US Naval Research Laboratory, Washington, DC 20375, USA

[3] Department of Mathematical Sciences, Durham University, Durham, DH1 3LE, UK

Abstract

We present an overview of results from a magnetofrictional model of the entire solar corona over a period of 47 yr. The simulation self-consistently reproduces decades of solar phenomena, varying in duration between rapid eruptions and the long-term solar cycles, from an input of observed active regions emerging at the photosphere. We have developed a geometric approach to use magnetic helicity to identify and localize the frequent eruptions that occur in the simulation. This method allows us to match our results to extreme-ultraviolet observations of transient events. We have analyzed the evolving magnetic topology by computing the squashing factor and segmenting the corona into discrete magnetic domains bounded by the Separatrix-Web. The simulations show a more dynamic structure to the Separatrix-Web than is predicted by potential field models, which may explain solar wind observations.

1. Introduction

Long-term studies of the solar corona typically approximate the magnetic field using the potential field source surface (PFSS) model (e.g., Wang et al. 2000; Virtanen et al. 2020; Luhmann et al. 2022), or the current sheet source surface (CSSS) model (Zhao & Hoeksema 1995; Koskela et al. 2019). PFSS assumes a current-free domain in which the field is at every time in a minimal-energy equilibrium. The key advantage of this approach is that the reconstruction can be performed uniquely from the observed radial magnetic field at the photosphere without knowledge of its prior history. The disadvantages are that transient, nonequilibrium events cannot be observed, and the morphology of magnetic streamers is unrealistic owing to the lack of coronal currents and imposed spherical source surface. CSSS improves the fit of PFSS with heliospheric observations by adding a single-parameter form of electric current, but retains the source surface and still cannot describe transients. By contrast, magneto-hydrodynamic (MHD) models can capture the full range of transient phenomena observed in the corona and better incorporate the solar wind boundary, but at such a prohibitive computational cost that decadal studies are not feasible.

Magnetofriction is an intermediate approach that replaces the MHD momentum equation with a simplified relaxation model while retaining the induction equation (for historical references see Yeates 2022). This means that magnetic flux conservation is incorporated so that the model retains a memory of previous interactions, in particular, the injection of magnetic energy and helicity into the closed-field corona by footpoint shearing. It has been applied on an active-region scale driven by observed high-cadence magnetograms to successfully form twisted magnetic flux ropes (Gibb et al. 2014; Lumme et al. 2022). More relevant here is its application on a global scale to model

the mean magnetic field in the corona evolving in response to active-region emergence and decay under supergranular convection and large-scale surface motions (van Ballegooijen et al. 2000; Yeates et al. 2008). Continuous simulations for a whole solar cycle (in fact 15 yr) were first run by Yeates & Mackay (2012), providing insight into the statistics of magnetic flux rope formation and eruptions (Lowder & Yeates 2017), and being used as a model for probing the magnetic topology of other stars (Lehmann et al. 2021).

Here, we extend magnetofrictional simulations to a continuous 47 yr period covering over four solar activity cycles during the space age for which regular magnetogram input data are available. From the PFSS and CSSS studies, it is known that there was significant variation in magnetic activity between these solar cycles, and this is also seen in observed rates of flares and coronal mass ejections (Hathaway 2015; Lamy et al. 2019). The longer-term goal of our work is to determine whether these variations are accurately reproduced by the magnetofrictional model, as well as what we can infer about possible activity in future (or past) cycles.

2. Numerical Methods

The Durham Magnetofrictional Code (DUMFRIC) is our present implementation of the model originally introduced by van Ballegooijen et al. (2000). Full model details and parameter values are given in Yeates & Bhowmik (2022). Briefly, the large-scale mean magnetic field $\boldsymbol{B} = \nabla \times \boldsymbol{A}$ is evolved in a three-dimensional spherical shell $R_\odot < r < 2.5\,R_\odot$ according to the mean-field induction equation,

$$\frac{\partial \boldsymbol{A}}{\partial t} = -\boldsymbol{E}, \quad \boldsymbol{E} = -\boldsymbol{v} \times \boldsymbol{B} + \boldsymbol{N}, \quad (1)$$

where $\boldsymbol{E}$ is the electric field and $\boldsymbol{v}$ is an artificial velocity,

$$\boldsymbol{v} = \frac{(\nabla \times \boldsymbol{B}) \times \boldsymbol{B}}{\nu B^2} + v_w \left(\frac{r}{2.5 R_\odot} \right)^{11.5} \hat{\boldsymbol{r}}. \quad (2)$$

The first term represents magnetofrictional relaxation toward a force-free equilibrium, where ν is the friction coefficient. The second term is a radial outflow to model the effect of the solar wind, where the wind speed at the outer boundary is $v_w = 100 \, \mathrm{km \, s^{-1}}$. The term N approximates the turbulent electromotive force (large-scale effect of small-scale turbulence) and uses a form of hyperdiffusion that conserves large-scale magnetic helicity. The computational grid in $(\log r, \cos \theta, \phi)$ consists of $61 \times 181 \times 361$ points.

The radial magnetic field at the inner boundary of the magnetofrictional simulation is initialized from a synoptic magnetogram. Thereafter, the tangential components of vector potential A are evolved using a surface flux transport model,

$$\frac{\partial \boldsymbol{A}_h}{\partial t} = -\boldsymbol{E}_h^{\mathrm{em}} + \boldsymbol{v}_s \times (B_r \hat{\boldsymbol{r}}) - \eta_0 \nabla \times (B_r \hat{\boldsymbol{r}}), \qquad (3)$$

where $\boldsymbol{v}_s(\theta)$ and η_0 represent imposed large-scale flow and supergranular diffusivity (details in Whitbread et al. 2017), and $\boldsymbol{E}_h^{\mathrm{em}}$ is an electric field imposed locally to emerge individual active regions (details in Yeates & Bhowmik 2022).

The $\boldsymbol{E}_h^{\mathrm{em}}$ for each region is chosen to generate a given radial magnetogram, for which we have assembled a curated database of emerging regions to be used by the model. Active regions were identified from synoptic magnetograms released by the Kitt Peak National Observatory (KPNO), the Synoptic Optical Long-term Investigations of the Sun, and the Helioseismic and Magnetic Imager. We have attempted to fill in data gaps during periods where these data sets overlap, if possible. Each emerging region injects a nonzero magnetic helicity ("twist") into the simulation volume, following the approach described by Yeates & Bhowmik (2022). Given the difficulty in estimating the individual magnetic helicities of all active regions over a 47 yr period, here we simply set the dimensionless twist parameter $\tau = 0.1$ for all regions in the northern hemisphere and $\tau = -0.1$ for all those in the southern hemisphere. The parameter study of Yeates & Bhowmik (2022) shows this to give roughly an upper bound for the amount of magnetic helicity in emerging regions. In their parameter study, halving $|\tau|$ reduced the (time-averaged) magnetic energy by about 6% and the mean electric current density by about 10%, but the outward helicity flux by about 50%, so this is an important parameter to calibrate in the future.

The DUMFRIC code makes use of magnetic helicity as a diagnostic tool for eruptive activity (Lowder & Yeates 2017; Bhowmik & Yeates 2021). The rate of change of the signed magnetic helicity in a given region of space ordinarily has contributions from nonideal dissipation in the bulk volume (very small) and flux through the enclosing surface of the region. For the sake of expediency, only the latter term is computed at the outer boundary at each time step, which in the "Weyl" gauge given by Equation (1), takes the form

$$\dot{H} = \int_S \boldsymbol{A} \times \boldsymbol{E} \cdot d\boldsymbol{S}. \qquad (4)$$

The instantaneous change in the helicity is saved at every time step (on the order of $\sim 5 \, \mathrm{s}$) during the simulation, to be used for identifying events such as eruptions. In principle, it would be preferable to compute $\dot{H}$ in the more physically meaningful "poloidal-toroidal gauge" (Berger & Hornig 2018; Yeates & Bhowmik 2022; Xiao et al. 2023). But this would be expensive at such high cadence and is unnecessary for the present study where we will be looking only at sudden and significant enhancements in $\dot{H}$, which will show up in (almost) any gauge. In order to localize the event to a particular spatial region, we also calculate the partial surface integral within a number of spherical caps, as demonstrated in Figure 1. A spherical cap is a dome-like structure formed by a planar cut through a sphere, or alternatively, a region of a spherical shell within a given distance of a point. We select a total of 18 caps over the outer simulation boundary, each one having an equal radius (at the base of the cap) of $0.6R_{\mathrm{SS}}$ (corresponding to a half-angle of $\sim 37°$ subtended from the Sun center), as shown in Figure 1(d). Note that the spherical caps in this arrangement overlap, so that each point on the outer simulation boundary is covered by between one and four adjacent caps; the sum total of magnetic helicity over all the caps typically differs from a surface integral over the outer boundary.

The magnetic field lines passing through a spherical cap above the solar equator during a quiet period on 2005 February 10 are shown in Figure 1(a). At a later time, during an eruption in this region, a "bird's nest" of twisted magnetic field lines is shown in Figure 1(c). The change in magnetic helicity through the illustrated spherical cap over a 3 day period, shown in Figure 1(b), exhibits a prominent peak. The timing of the peak itself corresponds to the erupting field lines passing through the outer boundary as they become disconnected from the photosphere. The formation of the eruption precedes the peak, as indicated by the second of the vertical blue lines in Figure 1(b). The full dynamics are also shown in the animated version of Figure 1.

This robust method allows the spatial and temporal identification of eruptive events in the present simulation. The method can be extended to any magnetohydrodynamic, magnetofrictional, or similar simulation by evaluating the integral in Equation (4) over appropriate spherical caps. This type of approach is particularly necessary for the type of long-term global simulation presented here because the solar activity is not localized by design, as in many magnetohydrodynamic simulations, for example. At high time cadence, it is a more efficient alternative to computing individual field line helicities (as in Lowder & Yeates 2017).

3. Results

The present simulation covers a period between 1975 September 25 and 2022 November 25, from solar cycle 21 to the start of cycle 25. The initial surface magnetic field was provided by a synoptic magnetogram from the KPNO. Thereafter, active regions emerged within the simulation as outlined above. Useful diagnostic quantities computed throughout the simulation volume were saved at every time step. The mean current density and total magnetic energy are shown in Figure 2. Both quantities have long-term trends that match the solar cycles and short-term spikes on the timescale of days. The spikes frequently correspond to the emergence of active regions but also occur as a result of the coronal dynamics outside the emergence of regions. The mean current gives an indication of the departure from the PFSS model, and consequently, transients in this quantity correspond to rapid reorderings of the magnetic field. In order to identify particular events, we compute a curve (yellow) that connects minima in the mean
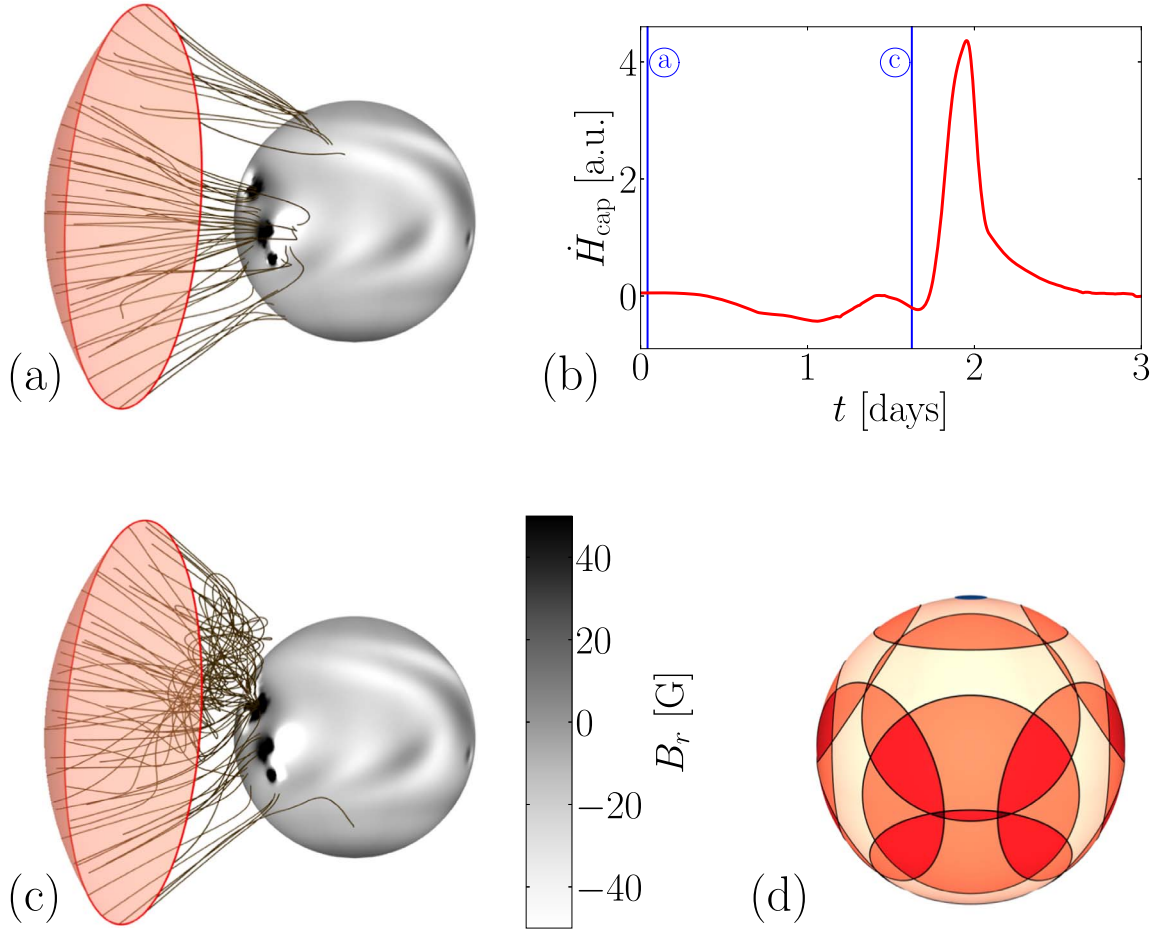
Figure 1. Snapshots of the magnetic field lines passing through a spherical cap (a) during a steady period and (c) during an eruption. The sphere at $R_\odot$ indicates the normal magnetic field at the photosphere. (b) The signed magnetic helicity change for this period, with the times of the snapshots indicated by blue lines. (d) The locations of the spherical caps (darker color indicates overlap) relative to the rotational axis of the Sun (blue, top). The animated version of this figure shows the 3 days of the simulation time period over a real-time duration of 15 s. Panel (a) is animated to show the changing field lines and normal magnetic field at the photosphere, while in panel (b) a moving blue line indicates the frame time relative to the signed helicity change. The magnetic field lines begin to twist and bunch up, as in (c), until the bunching is expelled from the simulation domain. A number of field lines remain disconnected from the photosphere until the steady configuration is recovered. Panel (d) is shown only in the static figure.

(An animation of this figure is available.)

current in such a way as to bound it from below, and therefore subtract a slowly varying background.

The spikes in the mean current and magnetic helicity over spherical caps have together been used to identify multiple eruptions. One such event that occurred on 2021 September 8 is shown in Figure 3. A typical closed-field configuration is seen at 19:00 on 2021 September 7 (Figure 3(a)), before the field lines visibly begin to open at 17:00 on 2021 September 8 (Figure 3(b)). The location corresponds closely to the emergence of active regions 12866 and 12868 within the simulation on the day of the eruption. The simulated eruption coincides with an observed eruption at around 17:30 on that day, as documented by the Heliophysics Events Knowledge-base[4]. The eruption is seen in an image from the Atmospheric Imaging Assembly of the Solar Dynamics Observatory (SDO; NASA[5]) taken at 17:28 (Figure 3(c)).

Another useful technique for visualizing the coronal magnetic field is the last closed flux surface (LCFS), the

three-dimensional separatrix between open and closed field lines. Before the eruption, the structure of the helmet streamer belt is visible in Figure 3(d). Thereafter, the LCFS begins to bulge outwards above the emerging active regions in Figure 3(e) as the closed field lines expand. The full dynamics are shown in the animated version of the figure, where the field line state is shown at each hour between 12:00 on 2021 September 7 and 12:00 on 2021 September 9 alongside the closest available image in time at the 191 Å wavelength. All of the visualizations in the static and animated versions of Figure 3 are oriented with respect to the Earth.

We note several limitations of the present magnetofric-tional simulations. The timing of the eruption in Figure 3 is tied closely to the emergence of the two active regions (which in our simulation are taken from synoptic maps), and therefore the match to the observations is fortuitous but atypical. Realistically, each active region causes multiple flares and eruptions that presently cannot be individually resolved by such a global model. It is typical of this DUMFRIC simulation to obtain a single sweeping eruption (as seen in Figure 3) for a time period with multiple entries in

---

[4] https://www.lmsal.com/hek/
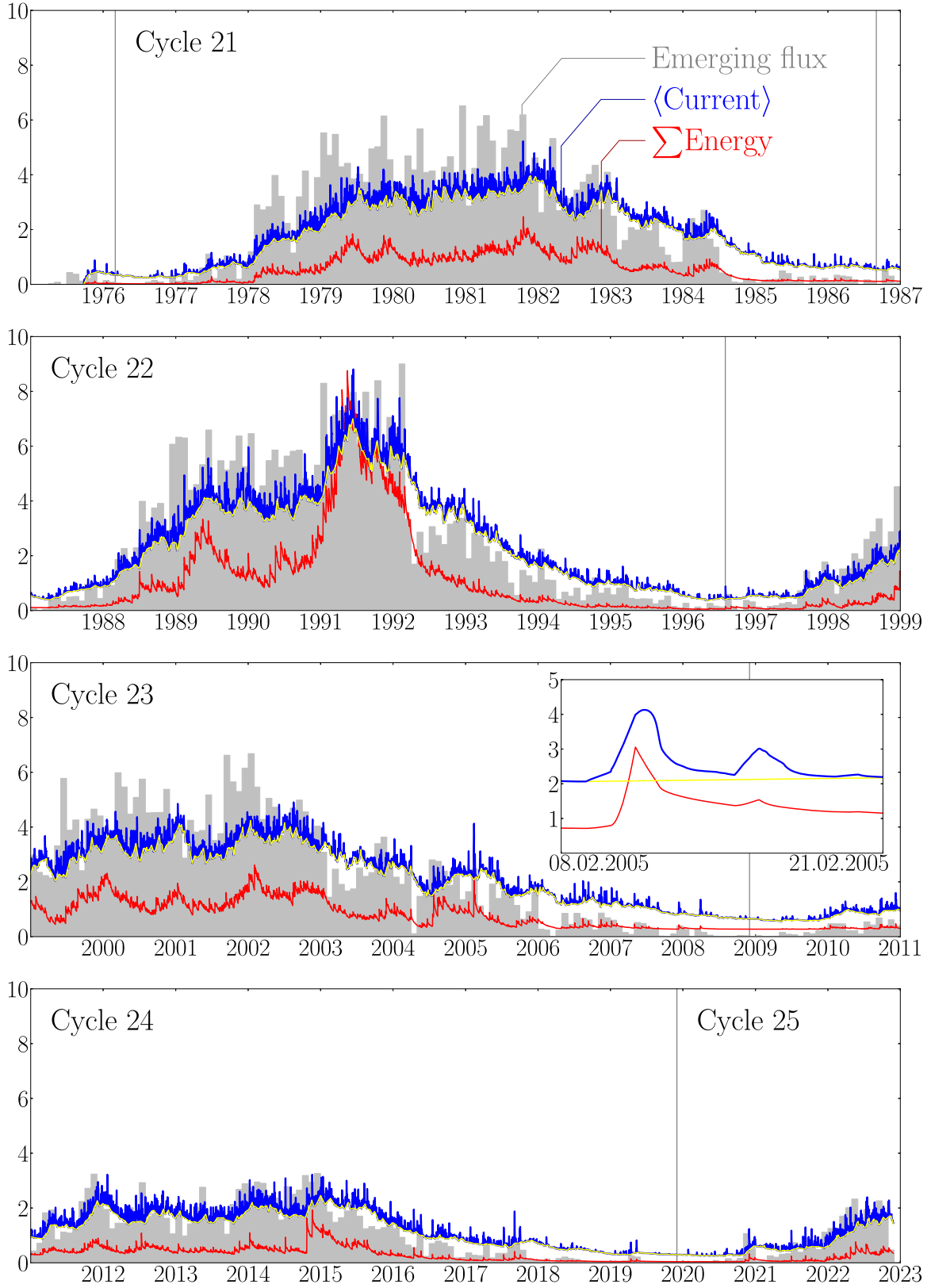[5] Images courtesy of NASA/SDO and the AIA, EVE, and HMI science teams.

Figure 2. Mean electric current density (blue) and total magnetic energy (red) through the domain over the simulation period, normalized to the same (arbitrary) peak value. The total flux of emerging regions on a monthly basis (also normalized) is shown in gray. The solar cycle number is indicated. The curve of the current is bounded from below by a slowly varying background (yellow). The inset at the end of Cycle 23 shows detail around the time period illustrated in Figure 1.

the Heliophysics Events Knowledgebase. Previous studies such as Yeates (2014) have also noted a lower eruption rate compared to observations. Eruptions also occur in

DUMFRIC—just as in reality—at times when no new regions are emerging. Nonetheless, the DUMFRIC code is able to reproduce many dynamic phenomena, such as
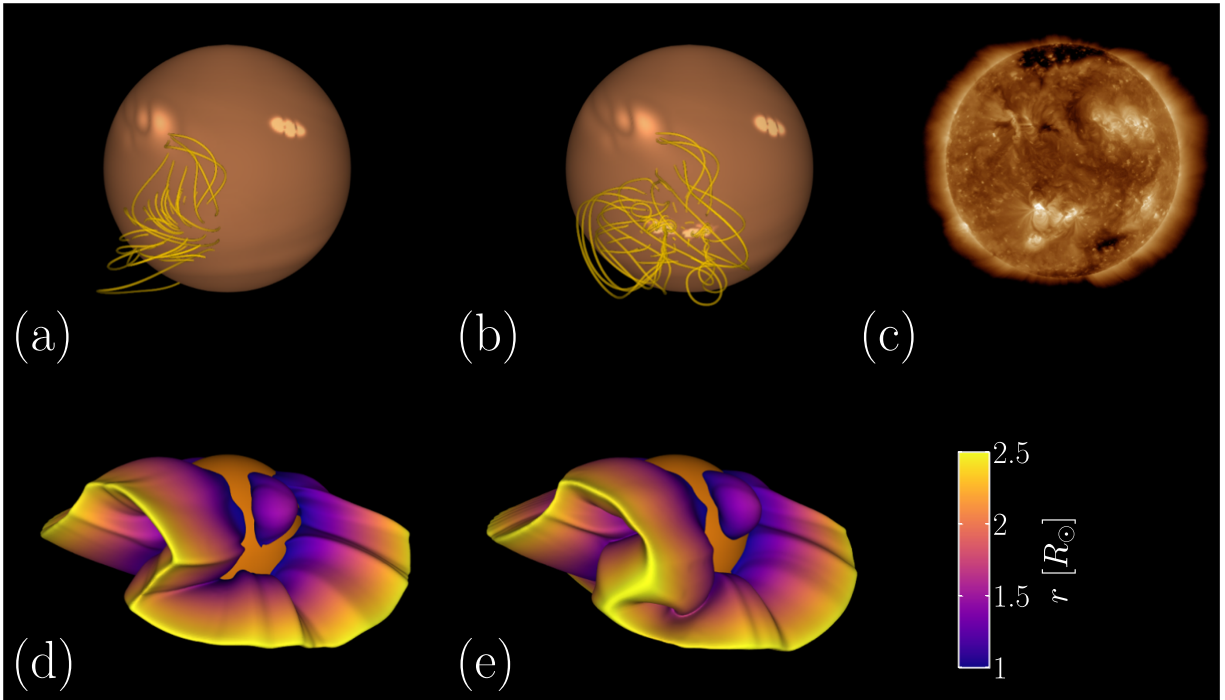
Figure 3. Magnetic field lines (a) 22 hr before and (b) during an eruption on 2021 September 8. (c) Extreme-ultraviolet image at 191 Å taken by SDO at 17:28 on 2021 September 8, during a peak in X-ray emission corresponding to an eruption. The associated bright region is visible below the midplane. Last closed flux surface (LCFS), separating open and closed field lines, (d) before and (e) during the eruption. The animated version of this figure shows hourly images of field lines and LCFS from our simulation alongside those 191 Å SDO images, which were taken at the closest point in time to each of the former. The animation runs from 12:00 on 2021 September 7 to 12:00 on 2021 September 9 over a real-time duration of 6 s. The animation depicts the rapidly expanding and opening field lines and a corresponding LCFS that balloons outwards. The relevant active regions brighten during the eruption time. The opened-up field lines straighten out and stabilize at the same time as the LCFS recedes.

(An animation of this figure is available.)

eruptions, magnetic flux ropes, and the build-up of electric current systems, which cannot be produced by the PFSS model. The long-term nature of the present simulation (which would likely pose a challenge for MHD models) will allow meaningful statistical trends to be identified.

The magnetic field computed by DUMFRIC exhibits a varying topology, which can elucidate open questions about the origin of the solar wind. A major source and driver of the solar wind, interchange reconnection between open and closed magnetic field lines, has been determined to occur continuously along the Separatrix-Web (Antiochos et al. 2011). We have computed the squashing factor Q using the QSL Squasher code (Tassev & Savcheva 2017) to investigate this S-Web. Formally, Q is bounded from below by the value of 2 and tends to infinity at discrete topological features such as separatrices and magnetic null points. This information, as well as additional information about the connectivity of the magnetic field, is encoded in the signed logarithm of Q, whose magnitude is equal to $\log Q$ but whose sign (positive or negative) specifies where the magnetic field is closed or open, respectively.

The squashing factor during a period of activity in solar cycle 22 is shown in Figure 4. Segmentation is performed on the squashing factor using the `HQVseg` code (Scott et al. 2018, 2019) to identify high-Q volumes (HQVs). These HQVs, particularly those connected to one or more magnetic nulls, are regions of space where interchange reconnection is likely to play a key part. Edwards et al. (2015) previously showed that the S-Web structure is significantly more complex in the magnetofrictional corona, compared to the PFSS model used in

most previous studies of the squashing factor. That work looked at isolated snapshots, but here we have calculated HQVs at 12 hr intervals over 6 days, demonstrating rapid variation in their location. We show the total time for which HQVs persist at $r = 2.5R_\odot$ in the lower panel of the static version of Figure 4 and their instantaneous locations in the animated version. From the former, it is evident that the S-Web exhibits rapid variation, particularly during a period of high solar activity (as can be seen from the mean current in the simulation at this time). The squashing factor calculated from the DUMFRIC magnetic field agrees with a PFSS model in the broad structure of the heliospheric current sheet and separatrices (such as areas with >5 days of HQV persistence) but adds dynamism to parts of the corona affected by emerging active regions (areas of lower HQV persistence). Future studies should compare this behavior with observations of eruptions, measurements of solar wind, eclipse images (as in Yeates et al. 2018), and MHD models.

4. Conclusion

We have performed one of the longest continuous and complete simulations of the solar corona using a magnetofrictional code. Aspects of long-term (such as solar cycles) and short-term solar activity (such as eruptions) are reproduced by the simulation. The simulated eruptions broadly match the timing, locations, and extent of observations, though the limited spatial resolution may mean that a single simulated eruption corresponds to multiple smaller observed events in the
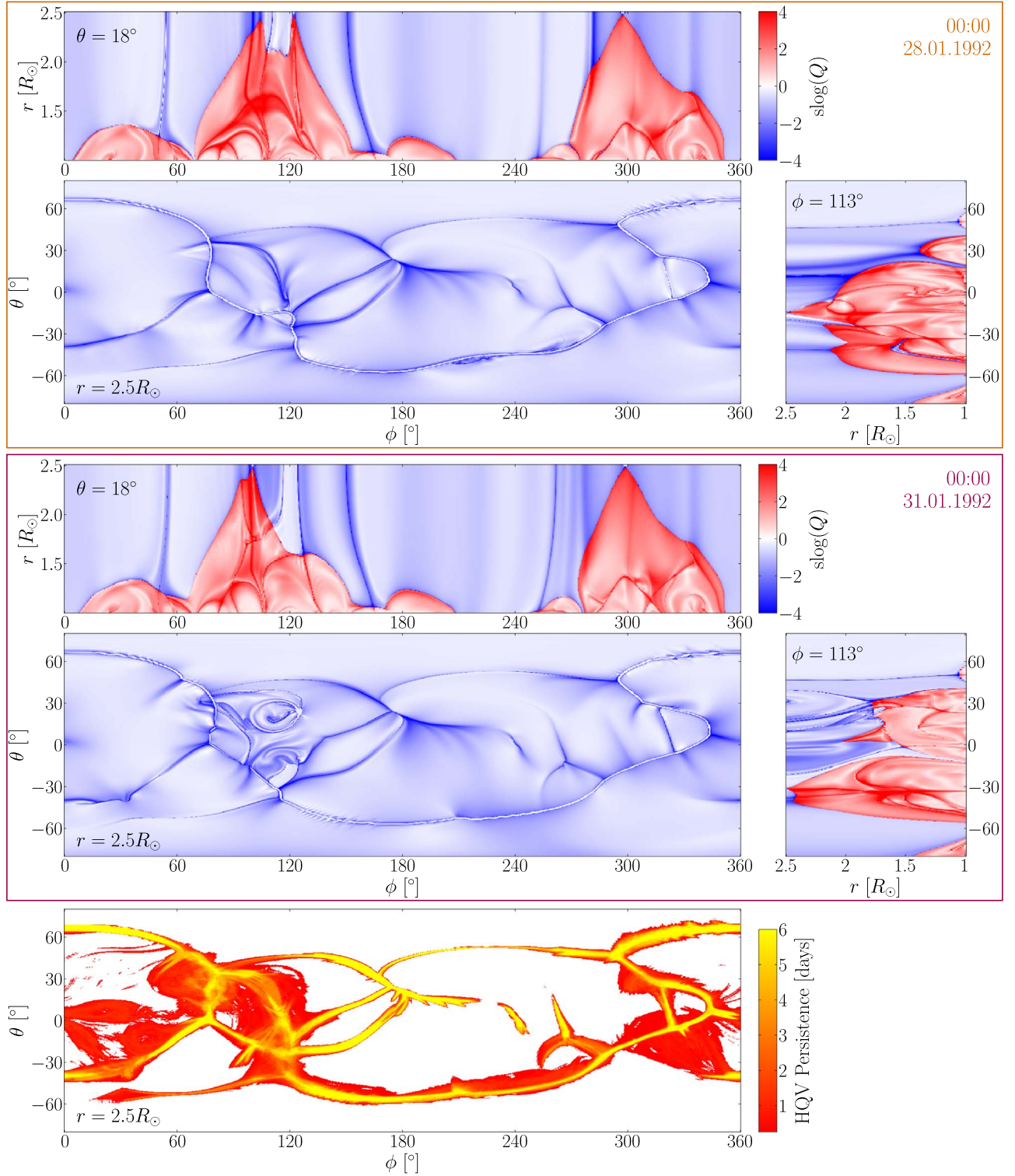
Figure 4. Separatrix-Web during the period 1992 January 28–1992 February 2. Signed logarithm of the squashing factor Q at constant r, θ, and ϕ as indicated on 1992 January 28 (upper panels) and on 1992 January 31 (middle panels). Positive (red) and negative (blue) values correspond to closed and open magnetic field lines, respectively. High-Q volumes (HQVs), which are likely sites of interchange reconnection, have been identified. The persistence in time of these HQVs is indicated (lower panel). The animated version of this figure shows how the squashing factor changes in 6 hr steps between 00:00 on 1992 January 28 to 18:00 on 2021 February 2 over a real-time duration of 16 s. The simulation time is annotated within the animation. The two helmet streamers in the cut at constant θ are seen to fill with high Q and open up in turn before relaxing. Corresponding folds appear in the slice at constant R and then straighten out. The bottom panel of the animation shows the instantaneous HQVs at each corresponding period in time. The HQVs show deviation from the long-term trend seen in the lower static figure.

(An animation of this figure is available.)

corresponding location. Further work must be undertaken to make a statistical comparison. A method for localizing eruptions using the outer boundary helicity flux, which could also be incorporated into more sophisticated models, has been described here. Existing methods of analyzing the magnetic field topology, which have previously been used largely for

force-free equilibria, have been adapted for these results. The data produced as part of this study are available upon request. We invite and encourage commentary from the wider solar physics community. Comprising the outputs are the magnetic field, current density, and plasma velocity. A suite of diagnostics is digitized at a high cadence.

ORCID iDs

Valentin Aslanyan https://orcid.org/0000-0003-3704-4229
Karen A. Meyer https://orcid.org/0000-0001-6046-2811
Roger B. Scott https://orcid.org/0000-0001-8517-4920
Anthony R. Yeates https://orcid.org/0000-0002-2728-4053

References

Antiochos, S. K., Mikić, Z., Titov, V. S., Lionello, R., & Linker, J. A. 2011, ApJ, 731, 112

Berger, M. A., & Hornig, G. 2018, JPhA, 51, 495501

Bhowmik, P., & Yeates, A. R. 2021, SoPh, 296, 109

Edwards, S. J., Yeates, A. R., Bocquet, F.-X., & Mackay, D. H. 2015, SoPh, 290, 2791

Gibb, G. P. S., Mackay, D. H., Green, L. M., & Meyer, K. A. 2014, ApJ, 782, 71

Hathaway, D. H. 2015, LRSP, 12, 4

Koskela, J., Virtanen, I., & Mursula, K. 2019, A&A, 631, A17

Lamy, P. L., Floyd, O., Boclet, B., et al. 2019, SSRv, 215, 39

Lehmann, L. T., Hussain, G. A. J., Vidotto, A. A., Jardine, M. M., & Mackay, D. H. 2021, MNRAS, 500, 1243

Lowder, C., & Yeates, A. 2017, ApJ, 846, 106

Luhmann, J. G., Li, Y., Lee, C. O., et al. 2022, SpWea, 20, e2022SW003110

Lumme, E., Pomoell, J., Price, D. J., et al. 2022, A&A, 658, A200

Scott, R. B., Pontin, D. I., & Wyper, P. F. 2019, ApJ, 882, 125

Scott, R. B., Pontin, D. I., Yeates, A. R., Wyper, P. F., & Higginson, A. K. 2018, ApJ, 869, 60

Tassev, S., & Savcheva, A. 2017, ApJ, 840, 89

van Ballegooijen, A. A., Priest, E. R., & Mackay, D. H. 2000, ApJ, 539, 983

Virtanen, I. I., Koskela, J. S., & Mursula, K. 2020, ApJL, 889, L28

Wang, Y. M., Lean, J., & Sheeley, N. R. J. 2000, GeoRL, 27, 505

Whitbread, T., Yeates, A. R., Muñoz-Jaramillo, A., & Petrie, G. J. D. 2017, A&A, 607, A76

Xiao, D., Prior, C. B., & Yeates, A. R. 2023, JPhA, 56, 205201

Yeates, A. R. 2014, SoPh, 289, 631

Yeates, A. R. 2022, GApFD, 116, 305

Yeates, A. R., Amari, T., Contopoulos, I., et al. 2018, SSRv, 214, 99

Yeates, A. R., & Bhowmik, P. 2022, ApJ, 935, 13

Yeates, A. R., & Mackay, D. H. 2012, ApJL, 753, L34

Yeates, A. R., Mackay, D. H., & van Ballegooijen, A. A. 2008, SoPh, 247, 103

Zhao, X., & Hoeksema, J. T. 1995, AdSpR, 16, 181